

Influence of interstitial Li on the electronic properties of $\text{Li}_x\text{CsPbI}_3$ for photovoltaic and battery applications

Wei Wei,^{1,2} Julian Gebhardt,² Daniel F. Urban,^{2,3} and Christian Elsässer^{1,2,3,*}

¹*Freiburg Center for Interactive Materials and Bioinspired Technologies,
University of Freiburg, Georges-Köhler-Allee 105, 79110 Freiburg, Germany*

²*Fraunhofer Institute for Mechanics of Materials IWM, Wöhlerstraße 11, 79108 Freiburg, Germany*

³*Freiburg Materials Research Center, University of Freiburg,
Stefan-Meier-Straße 21, 79104 Freiburg, Germany*

(Dated: December 2, 2025)

The integrated device of a perovskite solar cell with a Li-ion battery is an innovative solution for decentralized energy storage in smart electronic devices. In this study, we examine the stability of Li ions intercalated in a CsPbI_3 perovskite and their effect on the electronic structure of $\text{Li}_x\text{CsPbI}_3$ compounds using first-principles density functional theory. Our simulations demonstrate that the insertion of Li at concentrations up to $x = 1$ into CsPbI_3 perovskite is energetically possible. Moreover, we identify that the distortion of the Pb-I octahedra has the strongest impact on the change in the electronic band gap. Specifically, an increase in the amount of intercalated Li causes larger structural distortions, which in turn lead to an increasing band gap as function of the Li content.

I. INTRODUCTION

Advances in the design of smart electronic devices pose significant challenges for the integration and miniaturization of solar cells and energy storage components [1–4]. A promising approach involves the incorporation of halide perovskites as photovoltaic absorbers and Li-ion battery electrodes in commercial applications. Halide perovskites possess mixed ionic-covalent bonding character [5, 6], unlike the covalent or polar semiconductor compounds that are typically used in photovoltaic devices, and show good ionic conductivity [5]. Therefore, halide perovskite materials, which were originally designed for solar cells, may serve as multifunctional materials for both, light harvesting and Li storage.

The maximum amount of Li ions that can be stored in the unit cell of a perovskite crystal is determined by the quantity of available interstitial sites for the Li ions and their respective binding energies. Understanding and improving the performance of perovskite-based electrode materials for Li-ion batteries requires the knowledge of how the stability of materials is influenced by the intercalation of Li. Despite its importance, the interaction between inserted Li ions and the perovskite host crystal structure has not been studied extensively so far. Several experimental studies have looked at the structure and stability of Li-perovskite systems, and have reported a wide range of Li uptake limits of $x = 0 - 6$ in $\text{Li}_x\text{CsPbI}_3$ [7–10]. However, this wide range has not yet been comprehensively interpreted in the literature.

Furthermore, the insertion of interstitial elements always alters the electronic structure of the host crystal [11] which will have an influence on the performance of the solar cell [12]. While band gaps of Li-perovskite material systems have been measured experimentally [13, 14], the

relationship between the Li concentration and the band gap has not yet been systematically studied or explained.

In this work, we present a computational study based on density functional theory (DFT) to investigate the effects of Li-ion intercalation in $\text{Li}_x\text{CsPbI}_3$ as a prototype. CsPbI_3 is a well studied reference compound for inorganic halide-perovskite materials, with good light-harvesting capabilities [15–20]. We investigate two structural scenarios that serve as limiting cases for the dynamic CsPbI_3 perovskite structure under device-operation conditions [21]. The two cases, namely the cubic α structure and the distorted γ' structure, represent the highest saddle point configuration and the configurations at the local energy minima (when tetragonal lattice distortions are neglected) of the vibrating CsPbI_3 crystal, respectively. We study the Li uptake limit in the CsPbI_3 perovskite structure for both cases, and the influences of Li on the crystal and electronic structures of CsPbI_3 are systematically explored.

The paper is organized as follows. Sec. II introduces the computational setup and the definition of the formation energy of Li inserted into CsPbI_3 . In Sec. III, we present the results on the stability of interstitial Li within CsPbI_3 and its influence on the electronic structure. In Sec. IV, we discuss our results in view of other findings in the literature, and we summarize and conclude in Sec. V.

II. COMPUTATIONAL DETAILS

All calculations are carried out with the Vienna ab initio simulation package (VASP) [22] employing projector-augmented waves [23] and the strongly constrained and appropriately normed (SCAN) meta-generalized gradient approximation functional [24, 25]. An energy cutoff of 520 eV was used for the plane-waves basis. Total-energy differences and forces on atoms for all structural

* christian.elsaesser@iwmm.fraunhofer.de

degrees of freedom are converged within 1×10^{-5} eV and 5×10^{-3} eV/Å, respectively. The Brillouin-zone integrals were sampled by $4 \times 4 \times 4$ Monkhorst-Pack k -point grids [26] with a Gaussian smearing of 1×10^{-3} eV for the $2 \times 2 \times 2$ supercell models, containing 40 atoms (i.e., eight ABX_3 formula units). Structural relaxations for these systems are carried out in internal coordinates [27]. The implementation was improved to retain the initially set symmetry of the crystal.

To obtain accurate crystal structures, we combined the SCAN functional with the nonlocal correlation functional rVV10 [28] to account for van der Waals (vdW) dispersion interactions in our DFT calculations for the perovskite structures. Numerous authors have reported that the inclusion of vdW interactions in DFT calculations is useful to get quantitatively more accurate structural parameters for crystals, as compared to experimental data; see, e.g. the work of Xue et al. [29, 30] or other previous studies [31–33]. In our present work, the obtained values for the equilibrium lattice constant of CsPbI_3 are $a_0(\text{PBE})=6.39$ Å [21] and $a_0(\text{SCAN+rVV10})=6.27$ Å. The SCAN+rVV10 result agrees better than the PBE result with reported experimental data that vary from $a_0(\text{Expt.})=6.18$ Å to 6.30 Å [34–36].

The defect formation energies of Li ions intercalated at interstitial sites in the perovskite crystal are calculated as

$$E_{\text{form}} = \frac{E_{\text{tot}}[\text{Li}_x\text{CsPbI}_3] - E_{\text{tot}}[\text{CsPbI}_3] - x_{\text{Li}}E_{\text{tot}}[\text{Li}_{\text{bcc}}]}{x_{\text{Li}}}, \quad (1)$$

where $E_{\text{tot}}[\text{Li}_x\text{CsPbI}_3]$ is the total energy of the considered perovskite crystal containing Li, $E_{\text{tot}}[\text{CsPbI}_3]$ is the energy of the reference crystal without Li, $E_{\text{tot}}[\text{Li}_{\text{bcc}}]$ is the energy per Li atom in the body-centered cubic one-atom unit cell of the elemental Li metal, and x_{Li} is the proportion of Li per formula unit of the perovskite crystal. We assume that the perovskite crystal is in a Li-rich environment, i.e. in contact with a thermodynamic reservoir of metallic (body-centered cubic, BCC) Lithium. Therefore, the reference chemical potential is the energy per atom of the bulk BCC Li metal. The calculated lattice constant of BCC Li is 3.42 Å, and the total energy per atom of this metal was calculated using a $10 \times 10 \times 10$ Monkhorst-Pack k -point grid and otherwise the same computational parameters as for the perovskite.

For calculating the electronic structure, we employ the DFT+1/2 method [37] including spin-orbit coupling [38]. This method provides a similarly accurate electronic-structure description as hybrid-functional methods for CsPbI_3 perovskites, as demonstrated in our previous study [33].

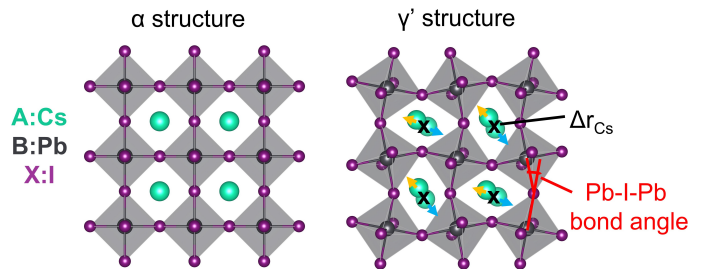


FIG. 1: The two limiting models of the dynamic crystal structure of CsPbI_3 , illustrating the degrees of structural distortion. The B-site atoms are located on the lattice points of the cubic (pseudo-cubic) structure. The off-center displacement of the A-site atoms (Δr_{Cs}) and the tilts of B-X octahedra described by the averaged Pb-I-Pb bond angle difference ($\Delta_{\text{Pb-I-Pb}}$) quantify the structural distortion.

III. RESULTS

A. The stability of interstitial Li in CsPbI_3

We studied two structural models, the α and γ' structures, to represent the two limiting cases of the dynamical CsPbI_3 phase at finite temperature. Figure 1 illustrates these two models. The ordered cubic α structure is observed as a temporal and spatial average in experimental studies [39, 40] and represents the highest saddle-point energy configuration of the phase, while the disordered γ' structure is obtained as the configuration of the local energy minimum of the α phase. Note that in reality the tetragonal lattice distortions towards the γ phase, which are observed at lower temperatures, are likely to occur in an averaged manner at higher temperatures, too. However, the influence of the concomitant small structural changes is weak, [21, 41] (e.g., the γ phase is more stable than the γ' structure by only 4.2 meV per unit cell) and, therefore, neglected for the remainder of this study. The structural difference between α and γ' can be attributed to two factors: the off-center displacement of the A-site Cs atoms (Δr_{Cs}), and the octahedral B-X tilts that occur around two axes [36] in the ABX_3 compound CsPbI_3 . Here, we quantify these octahedral tilts by the averaged Pb-I-Pb bond angle difference ($\Delta_{\text{Pb-I-Pb}}$).

In the following, we study the stability of interstitial Li as function of its concentration in the two structural models using a $2 \times 2 \times 2$ supercell. By subsequently adding Li to the two models, $\text{Li}_x\text{CsPbI}_3$ was obtained with Li concentrations varying from $x=1/8$ to $x=1$ for the α structure, and $x=1/8$ to $x=2$ for the γ' structure. We analyzed various different Li arrangements in the two models, as Li-Li interactions need to be considered for Li concentrations above the dilute limit.

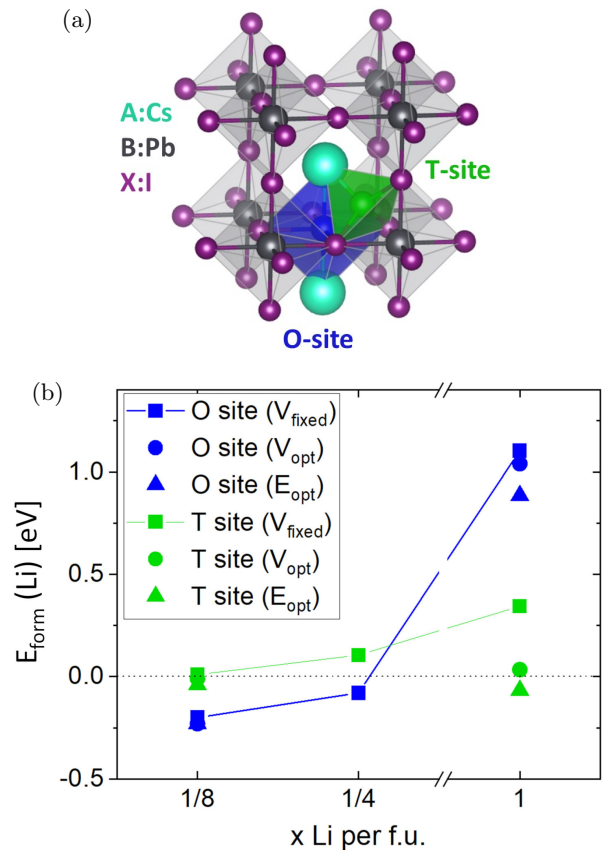


FIG. 2: a) Li interstitial sites in the α structure, located in the center of an octahedron (O) or a tetrahedron (T) formed by host lattice atoms. b) Formation energies of interstitial Li as function of the concentration x . The horizontal dotted line labels 0 eV. Square symbols indicate results obtained for a fixed simulation cell (V_{fixed}), circle symbols indicate that the volume of the cell was optimized, but the rectangular shape of the cell was maintained during optimization (V_{opt}), and the triangle symbols indicate structural relaxation in all degrees of freedom (E_{opt}). The point symmetry of the interstitial Li at the O site (D_{4h}) or T site (C_{3v}) is maintained for all Li concentrations.

1. The stability of interstitial Li in the α structure

In the α structure, the high-symmetry interstitial sites are three octahedral (O) and eight tetrahedral (T) sites as displayed in Figure 2a. The O site is located in the center of an octahedron formed by two Cs atoms and four I atoms, while the T site is located in the center of a tetrahedron formed by one Cs atom and three I atoms.

Figure 2b shows the formation energies of Li in both interstitial sites ranging from -0.20 to 1.10 eV for $x=1/8$ to $x=1$. We study the influence of varying the Li concentration x by: i) excluding changes to the lattice constant (V_{fixed}), ii) optimizing the volume (V_{opt}), and iii) allowing full relaxation of unit-cell degrees of freedom (E_{opt})

for each x . The highest point symmetry of a Li atom on an O site (D_{4h}) or a T site (C_{3v}) is maintained at every concentration x in all three cases.

For the fixed cell at low concentrations of $x=1/8$ and $x=1/4$, the insertion of Li atoms at the O sites is energetically more favorable by approx. 0.2 eV compared to the T sites. At $x=1/8$, the E_{form} on the O site is -0.20 eV, and an optimization of lattice degrees of freedom does not further stabilize the interstitial site. Increasing the concentration to $x=1/4$ rises E_{form} to -0.08 eV for the O site. In contrast, the results for $x=1$ differ significantly from those for the two lower concentrations. The order of E_{form} of the two sites is reversed and, compared to $x=1/4$, the formation energy of Li is increased by at least 0.42 eV (when changes in lattice parameters are excluded). Additionally, variations in lattice volume and shape have an influence on the E_{form} at $x=1$. Compared to keeping the volume fixed (V_{fixed}), allowing the volume to adjust to the Li content (V_{opt}) results in a stabilization of 0.06 eV for the O site and 0.31 eV for the T site (energy differences between square and circle symbols at $x=1$ in figure 2b), accompanied by an increase of the volume of 9% and 17%, respectively. Structural distortions away from the cubic structure, by relaxing all lattice parameters (E_{opt}) are energetically stabilized further by 0.016 eV for the O site and 0.10 eV for the T site (energy differences between circle and triangle symbols at $x=1$ in figure 2b). The lattice undergoes a tetragonal distortion with the insertion of Li at the O site, while the insertion of Li at the T site transforms the lattice into a rhombohedral cell with a cell-edge angle of 81° .

While the previous paragraphs apply to Li arrangements keeping the high symmetry of the host crystal structure, we now consider various Li arrangements at $x=1/4$ without enforcing any symmetry. The different arrangements of Li atoms influence their formation energy in the perovskite crystal. We observed that the formation energy is primarily associated with structural distortions of the host lattice, specifically characterized by a decrease of the formation energy with an increase of $\Delta_{\text{Pb-I-Pb}}$. This relationship even exceeds the changes concentration brings to the formation energy. As we observed in Figure 3, this relationship holds for all concentrations and Li arrangements investigated for the α structure. As the structural distortion increases, the α structure transforms to the γ' structure, accompanied by a decrease in the formation energy.

Therefore, the stability limit for interstitial Li in CsPbI_3 while maintaining the symmetry of the α structure is at $x=1/4$. For structures with $x=1/2$ it was impossible to maintain this high symmetry with any reasonable Li distribution.

2. The stability of interstitial Li in the γ' structure

Due to the lower symmetry of the γ' structure, compared to the α structure, the six O and eight T interstitial

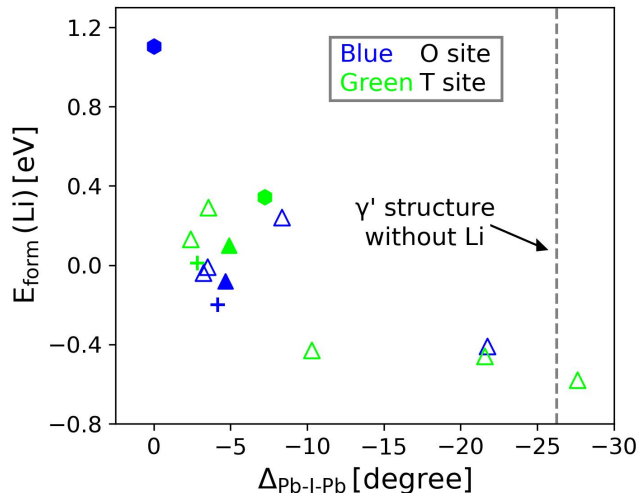


FIG. 3: The relationship between the formation energy of interstitial Li and the structural distortion $\Delta_{\text{Pb-I-Pb}}$ with varying Li concentration x in the α structure at fixed volume and cell shape. Blue and green symbols indicate interstitial Li on O and T sites, respectively. The different Li concentrations are indicated by these symbols: "+" for $x=1/8$, Δ for $x=1/4$, and \circ for $x=1$. Filled and open symbols represent high-symmetry and low-symmetry structures of the $\text{Li}_x\text{CsPbI}_3$ compounds, respectively.

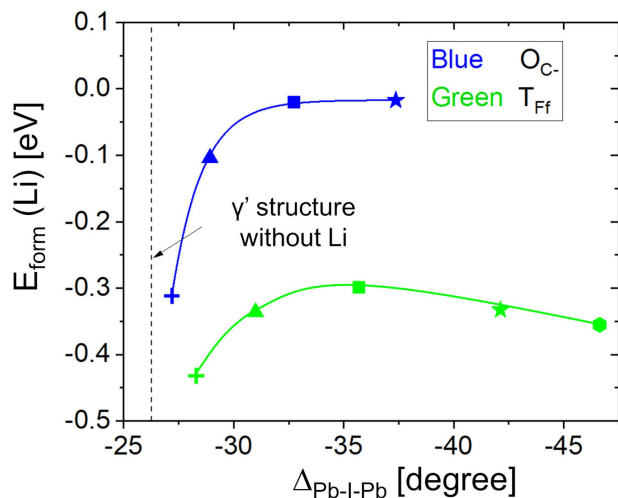


FIG. 4: The relationship between the formation energy of interstitial Li and the structural distortion $\Delta_{\text{Pb-I-Pb}}$ for the most stable O and T sites with varying Li concentration x in the γ' structure. The different Li concentrations are indicated by these symbols: "+" for $x=1/8$, Δ for $x=1/4$, \square for $x=1/2$, \star for $x=3/4$, and \circ for $x=1$.

sites are no longer symmetry equivalent. After optimization, the most stable T and O sites have formation energies of -0.43 and -0.31 eV per Li atom, respectively, in the 40-atoms supercell, i.e. at a Li concentration of $x=1/8$. We label these two most stable interstitial sites as T_{Ff} and $\text{O}_{\text{C-}}$ in accordance with the nomenclature introduced in our preceding work [21].

Figure 4 summarizes the Li formation energy of interstitial Li in the γ' structure for $x=1/8, 1/4, 1/2, 3/4$, and 1, on the T_{Ff} and $\text{O}_{\text{C-}}$ sites. In this model, the Li atoms are arranged as far away from each other as possible in the given supercell. Higher concentrations of Li consistently result in stronger structural distortions, but do not always lead to higher formation energies. From $x=1/8$ to $x=1/2$, the formation energy increases with increasing structural distortion $\Delta_{\text{Pb-I-Pb}}$. When x exceeds $1/2$, E_{form} reaches a peak. By further increasing x to 1 on T_{Ff} sites, a slight decrease of E_{form} is observed. However, Li is no longer stable on $\text{O}_{\text{C-}}$ sites in structures with $x=1$ and the Li atoms move to the neighboring T_{Ff} sites during the geometry optimization. The energy profile is again consistent with the γ' structure being the energetically most favorable structure. The minimum energy is obtained for a Li content of $x=1/8$ for which the resulting crystal structure is closest to the γ' structure.

To further explore the potential concentration limit for the intercalation of Li into the γ' structure, we investigate the Li concentrations up to $x=2$ at the T sites in the γ' structure. In this structure, three ways to insert and arrange the Li ions are followed. The different arrangements of Li ions may have different formation energies in the perovskite crystal. The crystal model is a $2 \times 2 \times 2$ supercell, comprising eight pseudo-cubic perovskite unit cells. Each cell is represented as a cubic cell marked by eight corner Pb atoms. Accordingly, these are the three arrangement ways: i) the "consecutive" arrangement means to add sequentially one atom to each cell until all eight cells contain one Li atom. And then, the procedure is repeated to add a second atom to each cell until all cells contain two Li atoms. ii) the "pair" arrangement stands for adding two Li atoms to the same cell at a time, followed by adding two atoms to another cell. This procedure is continued until all eight cells contain two Li atoms. iii) the "all in one unit" arrangement means to select a single cell and to add all Li atoms to that cell. In this arrangement, all Li atoms are concentrated in one cell, while the other seven cells remain devoid of Li atoms. Please note that our investigation here focuses on the potential concentration limit for Li in this perovskite crystal. It does not involve the methods of the process of inserting Li atoms or seek any controlled process to get a certain arrangement. The O sites are not considered in these arrangements because their formation energy is substantially higher, compared to that of the T sites. These strategies explore the stability of interstitial Li atoms from the most uniform to the most clustered Li distributions, which corresponds to the possibility of Li clustering in experiments.

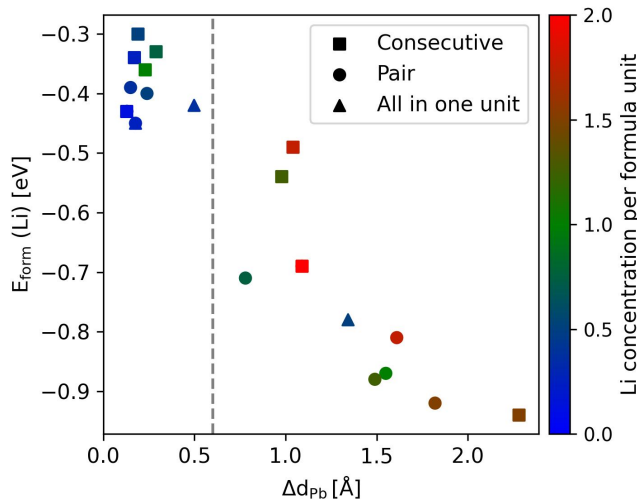


FIG. 5: The relationship between the formation energy of Li ions at T sites of the γ' structure and the concomitant distortion of the pseudo-cubic perovskite structure, for different Li concentrations up to $x=2$. The distortion is quantified by the average displacement of Pb atoms at B sites, and the Li concentration is illustrated by the color code. Formation energies for Li ions at O sites are not included in this figure because their values are considerably higher. The symbols denote consecutive (\square), pairwise (\circ) and all in one unit (\triangle) distributions of Li atoms, respectively. The vertical dashed line at $d=0.6$ Å distinguishes perovskite-type crystal structures for $d<0.6$ Å, which are weakly distorted by the inserted Li, from strongly distorted, no more perovskite-type crystal structures for $d>0.6$ Å.

Figure 5 illustrates the variation of the formation energy for different arrangements of Li with concentrations up to $x=2$. We observe a correlation between the formation energy and another type of lattice distortion. This lattice distortion can be quantified by the average displacement of Pb atoms from the B sites, denoted as Δd_{Pb} . The pseudo-cubic lattice of the perovskite structure is formed by Pb atoms located at the B sites, thus this average displacement serves as an indicator of the degree of distortion from the pseudo-cubic perovskite structure. In that structure, a chemical bond distortion may become clearly recognizable when the lattice length changes by more than 10%. Given that the lattice constant of the cubic perovskite structure is 6.27 Å, we set 0.6 Å as the threshold for Δd_{Pb} to indicate a significant distortion away from the pseudo-cubic structure. When this threshold is exceeded, the pseudo-cubic framework undergoes such a deformation that the structure can no longer be classified as perovskite-like. Although some high Li concentrations are energetically favorable, a detailed study of such non-perovskite-type structures would deviate from the focus of our research. In the figure, we have marked this threshold with a vertical gray dashed

line. Within the range that does not exceed this threshold, the concentration limit for Li uptake is found to be $x=1$. Any case with $x>1$ will have a severely deformed crystal structure. Hence, we infer that the concentration limit for the uptake of Li in the γ' structure of CsPbI_3 is $x=1$.

B. Electronic structure analysis

In the following we investigate the effect of interstitial Li atoms on the electronic band gap of the CsPbI_3 perovskite. We examine several factors, such as the Li-induced structural distortion, the electronic screening, and the defect states in the band gap related to the interstitial Li atoms. We limit the examined Li concentrations to $x \leq 1$ due to the instability of the perovskite structure for higher Li concentrations.

The relationship between the band gap E_g and the variation of the bond angle $\Delta_{\text{Pb-I-Pb}}$ for the α and γ' structures is illustrated in Figure 6a. We find a relationship between the two variables that appears linear across the high and low symmetry arrangements of Li in structures that were derived by adding Li into the α structure (red symbols). The structure with $x=1$ for the insertion of Li at the O site is an outlier, as it maintains the host crystal structure due to an artificially high symmetry. The band gap increases as the Li concentration rises. This growth trend is consistent with the earlier analysis of the structural distortion that arises when the Li content increases, i.e., increasing x leads to an increase of $\Delta_{\text{Pb-I-Pb}}$, which in turn increases E_g .

In the γ' structure, we observe a similar linear relationship between E_g and $\Delta_{\text{Pb-I-Pb}}$ (black symbols). However, the two linear regimes differ in slope and axis intercept.

The strong dependence of E_g on $\Delta_{\text{Pb-I-Pb}}$, which is in line with the different band gaps of the α structure (1.29 eV, $\Delta_{\text{Pb-I-Pb}}=0^\circ$) and the γ' structure (1.82 eV, $\Delta_{\text{Pb-I-Pb}}=-26^\circ$), indicates that the structural changes dominate the influence that interstitial Li atoms have on the electronic structure of CsPbI_3 . This is in line with the notorious sensitivity of band gaps in group-IV halide perovskite structures to the octahedral tilt angles [42].

To understand the direct effects of the insertion of Li atoms on the electronic structure of a CsPbI_3 crystal, we analyze the density of states (DOS) in the proximity of the band gap in Figure 7a. Upon the addition of Li to the α structure, the Fermi level (E_F) shifts to the edge of the conduction band for $x > 0$. An interstitial Li atom adds its $1s$ orbital as a deep core state (not shown). The Li $2s$ orbital remains mostly unoccupied, but hybridizes with Pb and I orbitals in the regions of the conduction and valence band edges (CBE and VBE), respectively. For small concentration x of Li, there is a significant distance of states with Li contributions to the two band edges (ΔE_{VBE} and ΔE_{CBE} , cf. Fig. 7b). With increasing x of Li, this distance shrinks, cf. Fig. 7c. This implies that Li affects the local environment of more I and

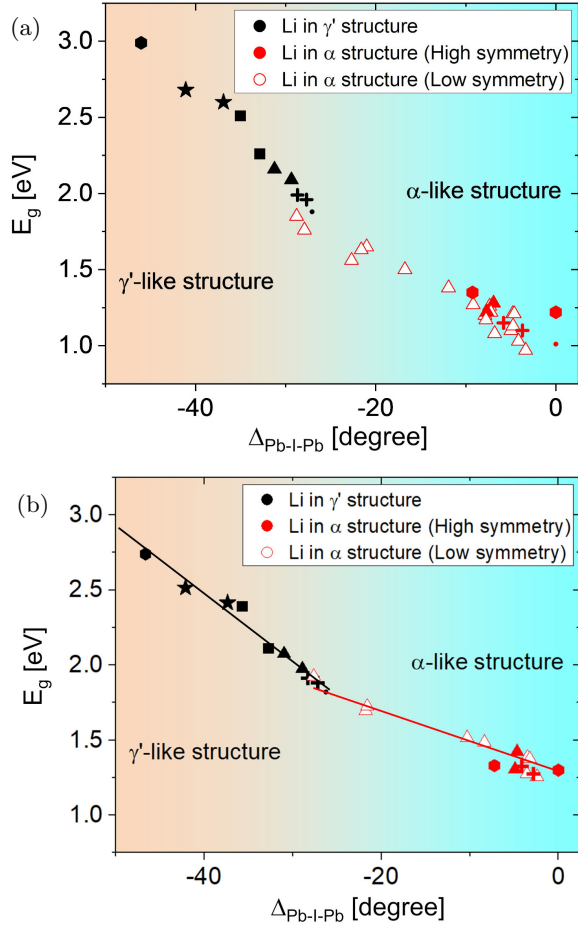


FIG. 6: (a) Band gap E_g vs. $\Delta_{\text{Pb-I-Pb}}$ for $\text{Li}_x\text{CsPbI}_3$ with different Li content x and Li distribution. Black and red symbols denote Li in the γ' and α structures, respectively. Orange and light blue colored areas indicate the structural regimes, respectively. Different concentrations are indicated as $x=0$ (●), $x=1/8$ (+), $x=1/4$ (Δ), $x=1/2$ (\square), $x=3/4$ (\star), $x=1$ (\circ). Filled symbols refer to structures that retain D_{4h} and C_{3v} symmetry for O and T sites in the α structure, respectively. Other lower symmetry arrangements of Li are indicated by open symbols. (b) Band gaps obtained after subtracting the influence of x extra electrons in the conduction band, estimated as $x \cdot 0.22$ eV (see text for details). The black and red lines are linear fitting to corresponding data points.

Pb atoms as the value of x increases. When Li atoms are located on the T sites, their contribution to the DOS has a broader distribution in energy, compared to Li atoms at the O sites at the same concentration. This indicates a stronger hybridization of Li with the Pb and I orbitals on the T sites than on the O sites.

We have also analyzed the DOS for various concentrations of interstitial Li in the γ' structure and obtain qualitative similarities to the findings for Li in the α structure. With a higher Li concentration, stronger structural

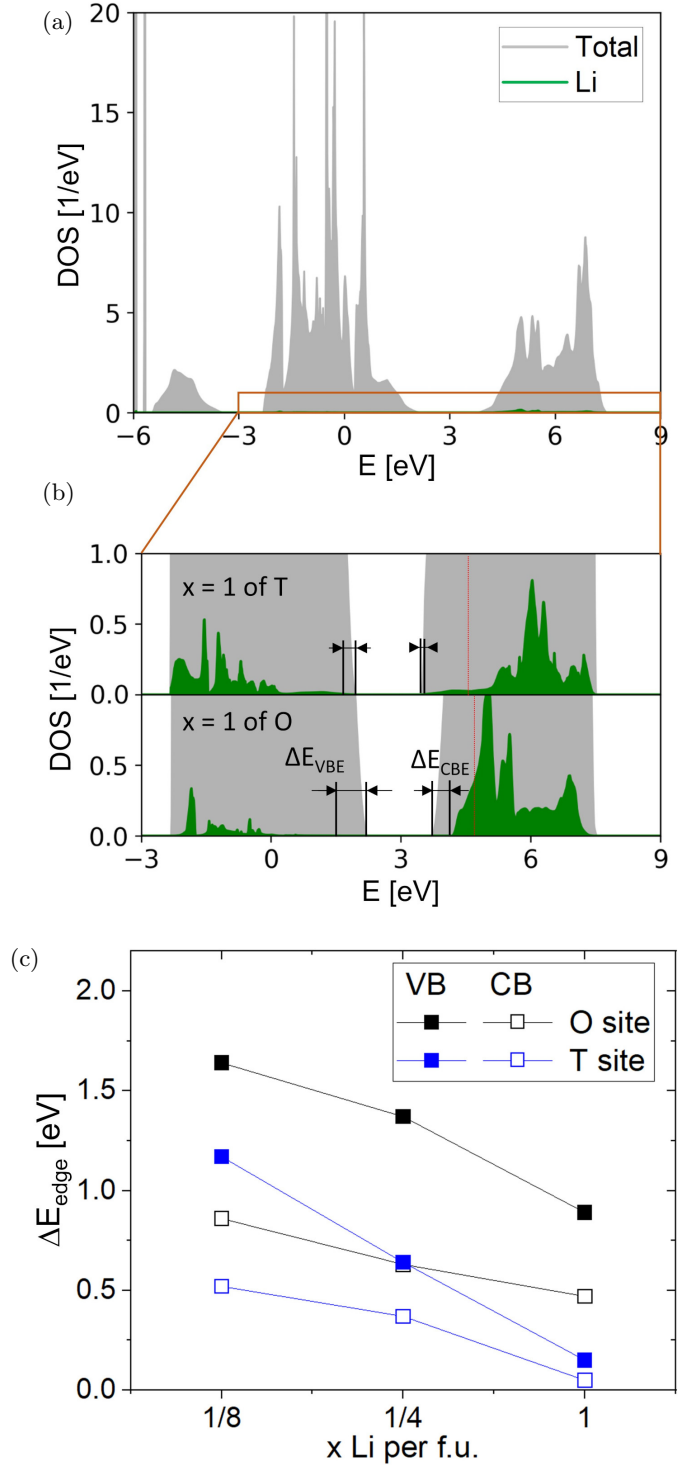


FIG. 7: (a) DOS of $\text{Li}_x\text{CsPbI}_3$ in the α structure and (b) the detailed DOS for interstitial Li on the O and T site with $x=1$. Structures with D_{4h} and C_{3v} symmetry are considered for O and T sites, respectively. Total DOS (gray) and Li projected DOS (green) are shown. E_F is indicated by red dashed lines and the energy separation of bands containing Li contributions from the two band edges, ΔE_{VBE} and ΔE_{CBE} , are marked by black lines and labels (c) The energy separation of bands with Li content from either band edge, ΔE_{edge} (edge: VBE or CBE), for $\text{Li}_x\text{CsPbI}_3$ with varying x in the α structure.

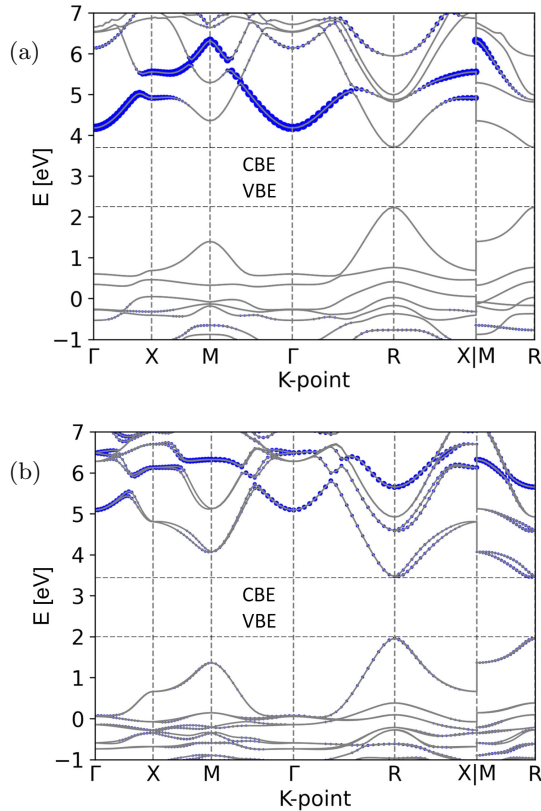


FIG. 8: Band structure of $\text{Li}_x\text{CsPbI}_3$ with Li atoms on the a) O and b) T sites for $x = 1$ in the α structure. Li contributions to bands are indicated by blue circles. The circle radius indicates the magnitude of the contribution.

distortions occur, resulting in a higher E_g . The Li $2s$ orbitals contribute to both the VBE and CBE at any concentration due to the stronger structural distortion, but their impact is still minor in magnitude.

Figure 8 displays the band structures of $\alpha\text{-Li}_x\text{CsPbI}_3$ with Li content $x=1$ at O and T sites to further analyze the hybridization between Li $2s$ orbitals and the host-crystal orbitals. The Li contribution to the bands is indicated by blue circles. When the Li atoms are located on O sites, the Li $2s$ states form a recognizable defect level (the bands with dense blue circles) that is more localized and has no contribution to the band edges. On the T site, the hybridization between Li $2s$ orbitals and Pb $6p$ orbitals occurs over a broader energy range.

The strength of the orbital overlap can be estimated based on the distances from Li to I and Pb. The nearest Li-I and Li-Pb distances of Li on T sites are 2.61–2.66 Å and 2.79–3.03 Å, respectively. For Li on O sites, the Li-I and Li-Pb distances are larger, 2.85–3.11 Å and 4.40–4.47 Å, respectively. As a result, the increased overlap estimated from the smaller spatial distance in case of the T site is consistent with a broadened Li $2s$ contribution that extends closer to the band edges for Li on T sites. However, in either case, the Li $2s$ contribution to

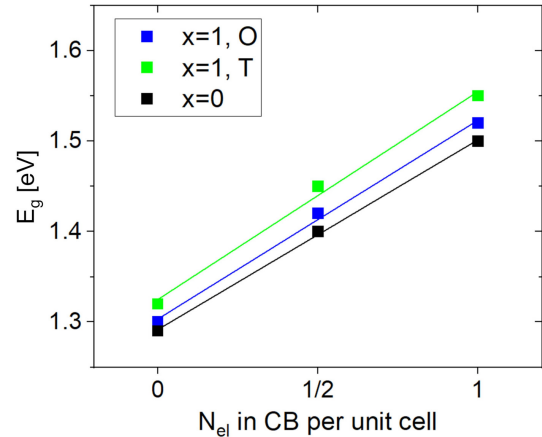


FIG. 9: Band gap change with varying number of electrons in the conduction band for three α structures of $\text{Li}_x\text{CsPbI}_3$ with $x = 0$ and $x = 1$ with Li atoms at O or T sites. The straight lines are linear fitting to the corresponding data points.

the band edges is negligible compared to the manifold of I and Pb states, cf. Fig. 7a.

So far, we have analyzed the case of inserting neutral Li atoms into the neutral perovskite crystal. Besides the $2s$ orbital, which appears to have a weak effect on the band edges, the insertion of a Li atom also introduces an additional electron into the CsPbI_3 crystal. In this scenario, the Fermi level (E_F) shifts into the conduction band, and the band gap of CsPbI_3 with Li in the O sites changes by 0.22 eV from $x = 0$ to $x = 1$, even without any structural alterations. This indicates that the extra electron in the conduction band directly influences the electronic structure. We quantify this effect in three different α structures, the one for $x = 0$ as well as the cases $x = 1$ with Li in O and T sites, respectively. Here, we keep the crystal structures unchanged when varying N_{el} .

The relationship between E_g and the number of excess electrons per perovskite formula unit, N_{el} , is illustrated in Figure 9. In all three investigated cases, the band gap increases with N_{el} ; this behavior is rather well described by a linear relation. The three slopes vary only between 0.21 and 0.23 eV per electron. This means that the influence of extra electrons at the CBE in $\text{Li}_x\text{CsPbI}_3$ alloys on the band gap can be modeled by an average shift of approximately 0.22 eV per extra electron.

We can use this relationship to subtract the influence of the extra charges by subtracting $x \cdot 0.22$ eV from the computed band gap values. Doing so, our computed structures serve as representative model structures for dilute $\text{Li}_x\text{CsPbI}_3$ alloys with very small x , where the structural changes of Li dopants occur locally, but the extra electrons may be delocalized. This description of this dilute limit is, however, not our main focus, having a battery application and, thus, large x in mind.

In the concentration range of interest, we can use the

above relation to isolate the structural influence on the band gap from the two influences of Li (extra electrons and band hybridization) that also contribute to the relation between E_g and $\Delta_{\text{Pb-I-Pb}}$.

The resulting behavior without the additional influence of extra electrons is displayed in Figure 6b. As noted above, the region of γ' -like structures is well represented by a linear relationship. Likewise, the structures with Li being added to the α structure are described well by a linear relationship. Accounting for the influence of a varying amount of extra electrons the outlier mentioned above for Li on the O site with $x=1$ fits well now to the linear relation.

We also analyzed a removal of all Li contributions, i.e., we determined the CsPbI_3 structures with the distortions caused by Li atoms, and then we removed the Li atoms when evaluating the electronic structure (i.e., the extra electrons, the $2s$ bands, and the ionic cores of Li are omitted). We find that the influence on E_g , coming only from the structural changes of the CsPbI_3 lattice in that way does only in some cases correlate well with the band-gap data given in Figure 6b. In about half of the cases, the interactions that are omitted when removing Li as bonding partner lead to significant changes in the local DOS of the Iodine p orbitals that are directed towards Li. Thus, the change of E_g with the Li content is dominated by the structural changes of the CsPbI_3 lattice, cf. Fig. 6a, and one can describe these changes by separating the structural effect from the varying amount of extra electrons in the conduction band, cf. Fig. 6b. But describing the observed band-gap variation purely by the structural changes of the CsPbI_3 lattice and neglecting the presence of Li as bonding partner is not successful.

IV. DISCUSSION

The ordered cubic α structure has served as the structural model of choice in most previous theoretical studies [16, 17, 43]. However, recent studies [33, 39, 40, 44] suggest that this model is probably not the preferred structural representation of the dynamic CsPbI_3 crystal around room temperature and the γ' structure is a more reasonable model. We find that the latter choice is even more relevant when adding Li to the structure, which itself promotes the occurrence of octahedral tilts in our results, cf. Fig. 3.

According to our simulation results, the limit for Li uptake into a hypothetical high symmetry α structure would be $x=1/4$, cf. Fig. 2. This is in line with the DFT results of Dawson et al. (from $x=0.037$ to $x=1$) on MAPbI_3 and MAPbBr_3 [10]. These results indicate that both hybrid halide perovskites cannot bear a Li concentration of $x=1$, and perovskite dissolution or distortion is energetically preferred. Similarly, Büttner et al. [7] reported that the electrolytes containing Li dissolve the perovskite immediately, and they concluded the impossibility to store Li ions in the hybrid halide

perovskites. This can be explained with the ability of the organic cations in hybrid perovskites to form hydrogen bonds to polar solvent molecules, which facilitates the perovskite decomposition [45]. This decomposition is even thermodynamically favorable for Pb-based hybrid halide perovskites [46]. In contrast, the inorganic CsPbI_3 perovskites are thermodynamically stable [46].

As opposed to the case of the α structure, the formation energy of interstitial Li in the γ' structure increases with increasing $\Delta_{\text{Pb-I-Pb}}$ for the most stable O and T sites at low Li concentration, cf. Fig 4. Thereafter, for $x=1/2$, the formation energy reaches a plateau, while the structural distortion still increases with increasing concentration. Overall, the energy profile is in line with a stabilization of the γ' structure, with the lowest energy obtained for the Li-containing structure that is closest to the γ' structure. The formation energies in a range from -0.43 eV to -0.30 eV (from $x=1/8$ to 1) indicate the potential for battery applications.

Higher Li concentrations with $x > 1$ disrupt the perovskite structure, altering the cubic lattice by the displacement of Pb (Δ_{dPb}) instead of only changing the Pb-I-Pb angles ($\Delta_{\text{Pb-I-Pb}}$), cf. Fig 5. This structural distortion differs significantly from the conditions of Li in the α structure and the lower Li concentrations in the γ' structure. We propose that it is unfeasible to maintain the perovskite structure in high concentrations of Li, whereby the limiting concentration of Li is $x=1$.

Interestingly, as the concentration of Li increases beyond $x=1$, the structural change is accompanied by a lower formation energy than for $x < 1$. It indicates a high capacity of the material for Li storage. Similar results have been reported for experiments [8, 9]. Xia et al. [8] demonstrated an astonishingly high Li concentration with $x \approx 6$ in $\text{Li}_x\text{MAPbBr}_3$, although the Li capacity faded rapidly after only 30 charge/discharge cycles. Vicente et al. [9] reported that the Li concentration in $\text{Li}_x\text{MAPbBr}_3$ reaches a value as high as $x = 3.7$. The rapid fading of the high Li capacity indicates structural distortion away from the perovskite structure, which is in line with our results for high Li concentrations.

Finally, we found that the insertion of Li increases the band gap of the CsPbI_3 perovskite, cf. Fig. 6. Similar results for Li containing perovskite compounds were reported from photoluminescence experiments [13, 14, 47]. Jiang et al. [13] found a blue shift in the photoluminescence spectrum by Li inserted in CsPbBr_3 , and attributed it to the Burstein–Moss effect [48]. This effect refers to the phenomenon that electrons at the VBE require higher energies to be excited due to the occupation of the CBE, thus exhibiting a higher absorption band gap. A similar blue shift was also found in $\text{Li}_x\text{MAPbBr}_3$ by Mathieson et al. [14]. They suggested that although the inserted Li atoms narrow the band gap, the electrons can only be excited by photons of higher energy due to the occupied CBE. However, the influence of the Li atoms on the band gap of the perovskite crystal is multifaceted, and the mechanism mentioned in the cited

literature is only about the occupied CBE. According to our results, the main reason for the increased band gap is the inevitable structural distortion induced by the Li atoms.

The band gap increase caused by the inserted Li is determined by the covalent bonding character of the halide perovskite. The VBE and CBE of CsPbI₃ are mainly composed of the covalent σ^* -bonding states of p and s orbitals of Pb and I [49], and the dispersion of the bands is determined by the overlaps of these orbitals. The insertion of Li atoms increases the $\Delta_{\text{Pb-I-Pb}}$ by attracting I atoms and, thus, reducing the overlap between the Pb and I orbitals. As a result, the presence of Li significantly increases the band gap, finally rendering three-dimensional halide-perovskite crystals not suitable for the use in photo-battery devices. But the organic-inorganic hybrid layers in two-dimensional perovskites may be more promising for Li storage and photovoltaic function. Ahmad et al. demonstrated the insertion of Li ions into a perovskite compound with a capacity of approx. 100 mAh/g and without compromising the photovoltaic efficiency [50]. Li is stored in the organic layer of the two-dimensional perovskite, which does not affect the band gap of the inorganic perovskite layer. Furthermore, Chen et al. [51] proposed a plausible Li storage mechanism involving carbonyl groups. The aforementioned mechanism (or related ones) holds the potential for developing an integrated halide-perovskite photo-battery.

V. SUMMARY

In this work, the structural stability of CsPbI₃ when Li is intercalated, and the effect that Li has on the electronic structure of the resulting Li_{*x*}CsPbI₃, are investigated. By exploring Li_{*x*}CsPbI₃ compounds with various concentrations and arrangements of Li ions, we find that structural distortions need to be considered for getting the Li formation energies to identify the Li concentration limit, and that the distortion of Pb-I-Pb bond angles is a more influential key feature for the band gap increase of Li_{*x*}CsPbI₃ materials than just the Li concentration.

We analyze the structural stability as function of the Li insertion by two structural models for CsPbI₃: first, the cubic perovskite α structure, which is a hypothetical

structure to be understood as a reference model with negligible probability to occur at room temperature; second, a distorted γ' structure, closely related to the γ phase, that represents the lowest energy structure at room temperature. The hypothetical α structure energetically disfavors Li uptake and is likely to be structurally unstable for $x > 1/4$. Thus, such a theoretical model is unsuitable for interpreting experiments that demonstrate the existence of Li_{*x*}CsPbI₃ compounds. In the γ' structure, interstitial insertion of Li is energetically favorable. Concentrations up to $x = 1$ are accessible while keeping the perovskite host structure intact. In principle, forming the compound with even higher Li concentration is feasible. However, our investigation of structures with up to $x = 2$ indicate that in such cases significant distortions of the host lattice structure occur. The structural distortions of such phase transitions and their potential irreversibility require further investigations.

For the concentration range $0 \leq x \leq 1$, the interstitial Li has several effects on the electronic structure of Li_{*x*}CsPbI₃: i) the induced structural distortion reduces the band dispersion, leading to a significant increase of the band gap; ii) the electronic screening of extra electrons in the conduction band leads to a slight increase of the band gap; iii) although the Li $2s$ orbitals hybridize with I and Pb orbitals, their effect on the band gap and the band edges is negligible.

Altogether, these effects result in an increased band gap in Li_{*x*}CsPbI₃ compared to CsPbI₃. The band gap E_g increases linearly with the induced averaged angle distortion $\Delta_{\text{Pb-I-Pb}}$ in the two structural regimes of the α and γ' models. For $x=1$, this leads to E_g of 2.96 eV. This continuously increasing band gap needs to be taken into account for potential solar cell applications.

ACKNOWLEDGMENTS

This work was supported by the Deutsche Forschungsgemeinschaft (DFG, German Research Foundation) under Germany's Excellence Strategy-EXC-2193/1-390951807 (LivMatS). We thank the State of Baden-Württemberg (Germany) through bwHPC for computational resources.

-
- [1] C. S. Lai, Y. Jia, L. L. Lai, Z. Xu, M. D. McCulloch, and K. P. Wong, A comprehensive review on large-scale photovoltaic system with applications of electrical energy storage, *Renewable and Sustainable Energy Reviews* **78**, 439 (2017).
 - [2] Y. Arora, C. Seth, and D. Khushalani, Crafting inorganic materials for use in energy capture and storage, *Langmuir* **35**, 9101 (2018).
 - [3] T. Berestok, C. Diestel, N. Ortlieb, S. W. Glunz, and A. Fischer, A monolithic silicon-mesoporous carbon photo-supercapacitor with high overall photoconversion efficiency, *Advanced Materials Technologies* **7**, 2200237 (2022).
 - [4] L. Zhang, J. Miao, J. Li, and Q. Li, Halide perovskite materials for energy storage applications, *Advanced Functional Materials* **30**, 2003653 (2020).
 - [5] Z. Li, C. Xiao, Y. Yang, S. P. Harvey, D. H. Kim, J. A. Christians, M. Yang, P. Schulz, S. U. Nanayakkara, C.-S. Jiang, et al., Extrinsic ion migration in perovskite solar cells, *Energy & Environmental Science* **10**, 1234 (2017).

- [6] J. Zhang, R. Chen, Y. Wu, M. Shang, Z. Zeng, Y. Zhang, Y. Zhu, and L. Han, Extrinsic movable ions in MAPbI₃ modulate energy band alignment in perovskite solar cells, *Advanced Energy Materials* **8**, 1701981 (2018).
- [7] J. Büttner, T. Berestok, S. Burger, M. Schmitt, M. Daub, H. Hillebrecht, I. Krossing, and A. Fischer, Are halide-perovskites suitable materials for battery and solar-battery applications—fundamental reconsiderations on solubility, lithium intercalation, and photo-corrosion, *Advanced Functional Materials* **32**, 2206958 (2022).
- [8] H.-R. Xia, W.-T. Sun, and L.-M. Peng, Hydrothermal synthesis of organometal halide perovskites for Li-ion batteries, *Chemical Communications* **51**, 13787 (2015).
- [9] N. Vicente and G. Garcia-Belmonte, Methylammonium lead bromide perovskite battery anodes reversibly host high Li-ion concentrations, *The Journal of Physical Chemistry Letters* **8**, 1371 (2017).
- [10] J. A. Dawson, A. J. Naylor, C. Eames, M. Roberts, W. Zhang, H. J. Snaith, P. G. Bruce, and M. S. Islam, Mechanisms of lithium intercalation and conversion processes in organic–inorganic halide perovskites, *ACS Energy Letters* **2**, 1818 (2017).
- [11] A. Willoughby, Atomic diffusion in semiconductors, *Reports on Progress in Physics* **41**, 1665 (1978).
- [12] C. H. Henry, Limiting efficiencies of ideal single and multiple energy gap terrestrial solar cells, *Journal of Applied Physics* **51**, 4494 (1980).
- [13] Q. Jiang, X. Zeng, N. Wang, Z. Xiao, Z. Guo, and J. Lu, Electrochemical lithium doping induced property changes in halide perovskite CsPbBr₃ crystal, *ACS Energy Letters* **3**, 264 (2017).
- [14] A. Mathieson, S. Feldmann, and M. De Volder, Solid-state lithium-ion batteries as a method for doping halide perovskites with an in situ optical readout of dopant concentration, *JACS Au* **2**, 1313 (2022).
- [15] S. Mahato, A. Ghorai, S. K. Srivastava, M. Modak, S. Singh, and S. K. Ray, Highly air-stable single-crystalline β -CsPbI₃ nanorods: A platform for inverted perovskite solar cells, *Advanced Energy Materials* **10**, 2001305 (2020).
- [16] J. Zhang, L. Yang, Y. Zhong, H. Hao, M. Yang, and R. Liu, Improved phase stability of the CsPbI₃ perovskite via organic cation doping, *Physical Chemistry Chemical Physics* **21**, 11175 (2019).
- [17] Y.-H. Kye, C.-J. Yu, U.-G. Jong, K.-C. Ri, J.-S. Kim, S.-H. Choe, S.-N. Hong, S. Li, J. N. Wilson, and A. Walsh, Vacancy-driven stabilization of the cubic perovskite polymorph of CsPbI₃, *The Journal of Physical Chemistry C* **123**, 9735 (2019).
- [18] J. B. Hoffman, A. L. Schleper, and P. V. Kamat, Transformation of sintered CsPbBr₃ nanocrystals to cubic CsPbI₃ and gradient CsPbBr_xI_{3-x} through halide exchange, *Journal of the American Chemical Society* **138**, 8603 (2016).
- [19] R. J. Sutton, M. R. Filip, A. A. Haghighirad, N. Sakai, B. Wenger, F. Giustino, and H. J. Snaith, Cubic or orthorhombic? Revealing the crystal structure of metastable black-phase CsPbI₃ by theory and experiment, *ACS Energy Letters* **3**, 1787 (2018).
- [20] B. Wang, N. Novendra, and A. Navrotsky, Energetics, structures, and phase transitions of cubic and orthorhombic cesium lead iodide (CsPbI₃) polymorphs, *Journal of the American Chemical Society* **141**, 14501 (2019).
- [21] W. Wei, J. Gebhardt, D. F. Urban, and C. Elsässer, Location and migration of interstitial Li ions in CsPbI₃ crystals, *Physical Review B* **109**, 144104 (2024).
- [22] G. Kresse and J. Furthmüller, Efficiency of ab-initio total energy calculations for metals and semiconductors using a plane-wave basis set, *Computational Materials Science* **6**, 15 (1996).
- [23] P. E. Blöchl, Projector augmented-wave method, *Physical Review B* **50**, 17953 (1994).
- [24] J. Sun, A. Ruzsinszky, and J. P. Perdew, Strongly constrained and appropriately normed semilocal density functional, *Physical Review Letters* **115**, 036402 (2015).
- [25] J. Sun, R. C. Remsing, Y. Zhang, Z. Sun, A. Ruzsinszky, H. Peng, Z. Yang, A. Paul, U. Waghmare, X. Wu, et al., Accurate first-principles structures and energies of diversely bonded systems from an efficient density functional, *Nature Chemistry* **8**, 831 (2016).
- [26] H. J. Monkhorst and J. D. Pack, Special points for brillouin-zone integrations, *Physical Review B* **13**, 5188 (1976).
- [27] T. Bučko, J. Hafner, and J. G. Ángyán, Geometry optimization of periodic systems using internal coordinates, *The Journal of Chemical Physics* **122**, 124508 (2005).
- [28] R. Sabatini, T. Gorni, and S. De Gironcoli, Nonlocal van der waals density functional made simple and efficient, *Physical Review B* **87**, 041108 (2013).
- [29] H. Xue, G. Brocks, and S. Tao, First-principles calculations of defects in metal halide perovskites: A performance comparison of density functionals, *Physical Review Materials* **5**, 125408 (2021).
- [30] H. Xue, J. M. Vicent-Luna, S. Tao, and G. Brocks, Compound defects in halide perovskites: A first-principles study of CsPbI₃, *The Journal of Physical Chemistry C* **127**, 1189 (2023).
- [31] H. Jing, R. Sa, and G. Xu, Tuning electronic and optical properties of CsPbI₃ by applying strain: A first-principles theoretical study, *Chemical Physics Letters* **732**, 136642 (2019).
- [32] M. A. Fadla, B. Bentría, T. Dahame, and A. Benghia, First-principles investigation on the stability and material properties of all-inorganic cesium lead iodide perovskites CsPbI₃ polymorphs, *Physica B: Condensed Matter* **585**, 412118 (2020).
- [33] J. Gebhardt, W. Wei, and C. Elsässer, Efficient modeling workflow for accurate electronic structures of hybrid perovskites, *The Journal of Physical Chemistry C* **125**, 18597 (2021).
- [34] G. E. Eperon, G. M. Paternò, R. J. Sutton, A. Zampetti, A. A. Haghighirad, F. Cacialli, and H. J. Snaith, Inorganic caesium lead iodide perovskite solar cells, *Journal of Materials Chemistry A* **3**, 19688 (2015).
- [35] D. Trots and S. Myagkota, High-temperature structural evolution of caesium and rubidium triiodoplumbates, *Journal of Physics and Chemistry of Solids* **69**, 2520 (2008).
- [36] A. Marrognier, G. Roma, S. Boyer-Richard, L. Pedesseau, J.-M. Jancu, Y. Bonnassieux, C. Katan, C. C. Stoumpos, M. G. Kanatzidis, and J. Even, Anharmonicity and disorder in the black phases of cesium lead iodide used for stable inorganic perovskite solar cells, *ACS Nano* **12**, 3477 (2018).
- [37] L. G. Ferreira, M. Marques, and L. K. Teles, Approximation to density functional theory for the calculation of band gaps of semiconductors, *Physical Review B* **78**,

- 125116 (2008).
- [38] S. Steiner, S. Khmelevskiy, M. Marsmann, and G. Kresse, Calculation of the magnetic anisotropy with projected-augmented-wave methodology and the case study of disordered $\text{Fe}_{1-x}\text{Co}_x$ alloys, *Physical Review B* **93**, 224425 (2016).
- [39] P. Whitfield, N. Herron, W. Guise, K. Page, Y. Cheng, I. Milas, and M. Crawford, Structures, phase transitions and tricritical behavior of the hybrid perovskite methyl ammonium lead iodide, *Scientific Reports* **6**, 1 (2016).
- [40] R. X. Yang, J. M. Skelton, E. L. Da Silva, J. M. Frost, and A. Walsh, Spontaneous octahedral tilting in the cubic inorganic cesium halide perovskites CsSnX_3 and CsPbX_3 ($X = \text{F}, \text{Cl}, \text{Br}, \text{I}$), *The Journal of Physical Chemistry Letters* **8**, 4720 (2017).
- [41] J. Klarbring, Low-energy paths for octahedral tilting in inorganic halide perovskites, *Physical Review B* **99**, 104105 (2019).
- [42] J. L. Knutson, J. D. Martin, and D. B. Mitzi, Tuning the band gap in hybrid tin iodide perovskite semiconductors using structural templating, *Inorganic Chemistry* **44**, 4699 (2005).
- [43] U.-G. Jong, C.-J. Yu, Y.-S. Kim, Y.-H. Kye, and C.-H. Kim, First-principles study on the material properties of the inorganic perovskite $\text{Rb}_{1-x}\text{Cs}_x\text{PbI}_3$ for solar cell applications, *Physical Review B* **98**, 125116 (2018).
- [44] J. Wiktor, U. Rothlisberger, and A. Pasquarello, Predictive determination of band gaps of inorganic halide perovskites, *The Journal of Physical Chemistry Letters* **8**, 5507 (2017).
- [45] C. Zheng and O. Rubel, Unraveling the water degradation mechanism of $\text{CH}_3\text{NH}_3\text{PbI}_3$, *The Journal of Physical Chemistry C* **123**, 19385 (2019).
- [46] Y. Zhou and Y. Zhao, Chemical stability and instability of inorganic halide perovskites, *Energy & Environmental Science* **12**, 1495 (2019).
- [47] H. Wu, J. Qiu, J. Wang, Y. Wen, Q. Wang, Z. Long, D. Zhou, Y. Yang, and D. Wang, The dual-defect passivation role of lithium bromide doping in reducing the nonradiative loss in CsPbX_3 ($X = \text{Br}$ and I) quantum dots, *Inorganic Chemistry Frontiers* **8**, 658 (2021).
- [48] E. Burstein, Anomalous optical absorption limit in InSb , *Physical Review* **93**, 632 (1954).
- [49] T. Umebayashi, K. Asai, T. Kondo, and A. Nakao, Electronic structures of lead iodide based low-dimensional crystals, *Physical Review B* **67**, 155405 (2003).
- [50] S. Ahmad, C. George, D. J. Beesley, J. J. Baumberg, and M. De Volder, Photo-rechargeable organo-halide perovskite batteries, *Nano Letters* **18**, 1856 (2018).
- [51] Y. Chen, Z. Chen, X. Zhang, J. Chen, and Y. Wang, An organic-halide perovskite-based photo-assisted Li-ion battery for photoelectrochemical storage, *Nanoscale* **14**, 10903 (2022).